Energy Storage Materials 62 (2023) 102936

Contents lists available at ScienceDirect

Energy Storage Materials

journal homepage: www.elsevier.com/locate/ensm

Unlocking the chemical space in anti-perovskite conductors by incorporating anion rotation dynamics

Chaohong Guan [a], Yu Yang [a], Runxin Ouyang [a], Huirong Jing [a], Jieqiong Yan [a], Guoyao Li [b], Huanan Duan [b], Hong Zhu [a,*]

[a] University of Michigan–Shanghai Jiao Tong University Joint Institute, Shanghai Jiao Tong University, Shanghai 200240, China
[b] State Key Laboratory of Metal Matrix Composites, School of Materials Science and Engineering, Shanghai Jiao Tong University, Shanghai 200240, China

ARTICLE INFO

Keywords:
Lithium anti-perovskite electrolytes
Cluster-dynamics
Paddlewheel dynamics
Local difference frequency center

ABSTRACT

Anti-perovskite compounds have drawn significant research interest as promising next-generation electrolytes for solid-state batteries, due to the high chemical stability against Li-metal, the negligible electronic conductivity and low cost. However, the low ionic conductivity, and the deficient fundamental understandings of ion transports impede the further optimization of the lithium anti-perovskite electrolytes. Herein, we reveal that exchanging anion lattice sites in the anti-perovskite could promote the structure stabilities and ionic conductivities simultaneously, by incorporating the rotational dynamics of anion clusters and strengthening the coupling between Li migrations and cluster rotations. Based on high-throughput calculations by density functional theory (DFT), twelve new anti-perovskite materials are predicted to exhibit superionic conductivity, among which the highest ionic conductivity of 10.9 mS/cm in Li_3BrSO_4 can be achieved (hundreds of times higher than the ionic conductivity of typical Li_3OCl antiperovskite, 0.021 mS/cm). Furthermore, the local difference frequency center is proposed to quantitatively characterize the coupled degree of Li migration and cluster rotation, revealing the contribution of paddlewheel effect to the ionic conductivity. Our proposed cation-anion dynamics coupling in site-exchanged and cluster-based antiperovskites not only open a new avenue for understanding the key role played by rotational dynamics on fast lithium mobility, but also can be generally applied to develop other fast ionic conductors with cluster dynamics.

1. Introduction

As the promising next-generation energy storage technology, solid state batteries have garnered increasing attention attributing to the intrinsic safety and potential opportunities to realize long-life cycle and high-energy density [1,2]. In recent years, tremendous endeavors were made on the development of solid-state electrolytes (SSE) with high ionic conductivities at room temperature (RT), comparable to that of liquid electrolytes in conventional lithium-ion batteries ($\sim 10^{-2}$ S cm^{-1}) [3]. The ionic conductivities of state-of-the-art SSEs can reach the order of 10^{-3} – 10^{-2} S cm^{-1}, such as sulfides SSEs ($Li_{10}GeP_2S_{12}$, σ_{RT} = 12 mS/cm) [4], garnets ($Li_7La_3Zr_2O_{12}$, σ_{RT} = 1–2 mS/cm) [5], argyrodite-type SSEs ($Li_{6.72}PS_5Cl$, σ_{RT} = ~1 mS/cm [6], while the latest reported argyrodite-type $Li_{6.25}PS_{5.25}(BH_4)_{0.75}$ exhibits the theoretical highest ionic conductivity of 177 mS cm^{-1} at RT [7]) and anti-perovskite SSEs ($Li_3OCl_{0.5}Br_{0.5}$, σ_{RT} = 1–2 mS cm^{-1}) [8]. Although significant progress has been made over the past decade in enhancing ionic conductivity of SSEs by experiment and theoretical simulations, few experimentally or even theoretically reported SSEs so far, such as $Li_{6.25}PS_{5.25}(BH_4)_{0.75}$ and $Li_{1+2x}Zn_{1-X}PS_4$ [9], exhibit the ionic conductivity comparable to that of the so-called advanced superionic conductors (ASIC, whose ionic conductivity is close to 100 mS /cm at RT, and the activation energy is about 0.1 eV) [10]. This ASIC was found in the field of iodide fast ionic conductor four decades ago, e.g., $RbCu_4Cl_3I_2$, which shows the superionic Ag^+ and Cu^+ diffusion [11]. Therefore, seeking novel SSEs with higher ionic conductivity at RT that can reach or come close to the criteria of ASIC is desirable and valuable for further improving the performance of lithium solid state batteries. As reported in previous works, the enhanced ionic conductivity of SSEs facilitates to increase active materials loading in the cathode materials, decrease the build up of mechanical stress in the lithium anode and reduce the overall impedance in the solid-state batteries [12,13].

For realizing the superionic conductivity at RT in the lithium conductors, the fundamental understanding of the structural features and

* Corresponding author.
E-mail address: hong.zhu@sjtu.edu.cn (H. Zhu).

https://doi.org/10.1016/j.ensm.2023.102936
Received 20 May 2023; Received in revised form 18 July 2023; Accepted 18 August 2023
Available online 19 August 2023
2405-8297/© 2023 Elsevier B.V. All rights reserved.

mechanisms that determine the ability of lithium-ion migration worth pursuing from the perspectives of experiment and theory to accelerate the design of new SSEs. For example, the superionic conductivities of sulfide-based electrolytes could originate from the body-centered-cubic (bcc) arrangement of anions, which provides lithium migration pathways with low energy barriers between face-sharing tetrahedral sites [14]. This structural feature also has been adopted as screening criterion to find new fast ionic conductors, e.g. $Li_{1+2x}Zn_{1-X}PS_4$ with the ultra-high theoretical RT conductivity of 114 mS/cm [9]. Besides, concerted migration of lithium atoms with a decreased activation energy has been observed in some sulfide (LGPS, $Li_7P_3S_{11}$, etc.), oxide (LLZO, LLTO, etc) and other fast ionic conductors [15–18]. In spite of the concerted migration found in the oxides, the ionic conductivity of which is lower than that of sulfides, Ceder's group reported the corner-sharing structural feature as a new descriptor to screen the oxide fast ionic conductors, theoretically guiding the design of new oxide superionic conductor ($LiIn(IO_3)_4$, $\sigma_{RT} = 18$ mS cm^{-1}) [19].

More recently, the solid electrolytes containing anion clusters, such as Li_3OBH_4, Li_2OHCl, $Li_2B_{12}H_{12}$, Li_3SBF_4, $Li_6POS_4(SH)$, $Li_6PS_5(BH_4)$, $Na_3S(BCl_4)$, β-Li_3PS_4, Na_3OBH_4, etc. are attaining a lot of research interests [7,18,20–24], especially due to the thermally-activated dynamics coupling between migrating cations and rotational anion clusters. The disordered reorientations of anion clusters could assist the migration of lithium ions with the low activation energy, so-called the paddle-wheel effect. The $Li_6POS_4(SH)$ and $Li_6PS_5(BH_4)$ argyrodite-type SSEs [7] show the anomalously high ionic conductivities at RT ($\sigma_{RT} = 82$ mS/cm and 177 mS/cm, respectively, with the SH^- and BH_4^- exhibiting the faster rotational dynamics than that of the $B_{12}H_{12}^{2-}$ and PS_4^{3-} clusters in the $Li_2B_{12}H_{12}$ and Li_3PS_4). Therefore, the existence of clusters enjoying great rotation freedoms is necessary for the paddle-wheel-effect enabled high ionic conductivities.

Here, motivated by the great potential of paddle-wheel effect on optimizing ionic conductivity of SSEs, we have studied the cluster-based anti-perovskite materials based on the density functional theory (DFT) simulations to break the limitation of low ionic conductivities of experimentally existing anti-perovskite (AP) SSEs. For the typical anti-perovskite Li_3AB (A represents divalent chalcogen anions and forms the corner-sharing Li_6A octahedra, and B represents monovalent halogen anions and occupies the space between octahedra), the reported ionic conductivities are about 1 mS/cm [25]. While there are limited number of A-B pairs to form stable Li_3AB, impeding the further exploration of anti-perovskite SSEs. Considering the stability based on the tolerance factor (t) of perovskite structures, we exchanged the positions of A and B anions to obtain modified-Li_3BA with suitable t. Among these structures, the Li_3BrSO_4 exhibits the highest RT ionic conductivity of 10.9 mS/cm and the lowest activation energy of 0.22 eV, which mainly attributes to the high rotational degrees of freedom for anion clusters and the reinforced paddlewheel dynamics. According to the systematic study of the cation-anion coupling dynamics, our findings uncover the ion-conduction mechanisms for the fast-ion diffusion in the modified-Li_3BA materials and suggest that the degree of paddlewheel dynamics could be evaluated by the difference between the local cluster rotational frequency and Li hopping frequency, namely the local difference frequency center.

2. Computational methodology

2.1. First-principles structure search for the cluster-based anti-perovskites

The structures of cluster-based APs were predicted by the global minimum search of free energy surfaces via DFT calculations based on the particle swarm optimization algorithm implemented in the CALYPSO [58]. The cluster gas-phase structures (Fig. S1) are regarded as a single element and introduced to the initial structures of the APs. As to search the ground-state structure of Li_3ClSO_4, three elements (Li, Cl and SO_4) are adopted to build the trial structures containing one formula unit. During a regular search, a population with 20–30 initial structures are generated according to different space groups, then these structures are fully optimized until the energy and force convergence criteria of 10^{-5} eV and 0.03 Å/eV are reached, respectively. The 60% of the optimized structures with the ranked lowest energies were used to build the next generation with the updated structures based on different symmetries. When the lowest energies of structures do not change after 10–30 generations of optimization, the structures are picked out for the further studies.

2.2. Calculations of the properties of the cluster-based anti-perovskites

The DFT calculations in this work were carried out by the VASP package based on the projector augmented wave (PAW) method [59]. The Perdew-Burke-Ernzerhof (PBE) generalized gradient approximant (GGA) was applied to describe the exchange-correlation potential for the overall structural optimization with a 7*7*7 Monkhorst-Pack k-point mesh. The energy cutoff for plane wave expansion is 550 eV, and the energy and force convergences are set to 10^{-6} eV and 0.01 eV/Å, respectively. The phonon dispersions were calculated by the Phonopy package [60] based on Density Functional Perturbation theory (DFPT) [61]. To prevent the presence of abnormal imaginary frequency in the dispersive spectrum, the higher convergence criteria of energy (1×10^{-10} eV) and force (10^{-8} eV $Å^{-1}$) are applied during the structure optimization. Additionally, the electronic structures were calculated based on HSE06 hybrid functional [62]. Additionally, the ab initio molecular dynamics (AIMD) was used to investigate the ionic conductivities, the detailed can be found in section S1 of the supporting information.

2.3. Procedure for fitting the moment tensor potential

MTP was fitted to evaluate the Li diffusion at room temperature. The trained and tested data were prepared based on the AIMD simulations. During this AIMD simulations, time step was set to 2 fs, and all supercell systems were simulated for a short time with a total of 10,000 steps at different temperatures (from 300 to 1100 K with 200 K intervals). For each temperature, about 300 snapshot structures were uniformly extracted from the production run of 20 ps. Hence, a total of 1500 training structures were generated. To obtain accurate energies and forces for machine learning potential training, the static self-consistent field calculations for the training structures were carried out. These SCF calculations were performed with a higher k-point density of at least 100/$Å^{-3}$, an energy cutoff of 520 eV. The convergence criterion of energy for SCF calculations was set to 10^{-6} eV/atom. During the MTP model training, the energy and force data points are assigned weights of 100:1, similar to the previous work by S.P. Ong [63]. And an 80:20 split of the training:test data was used. All training and simulations with MTP framework were performed by using the open-source software and Python packages, including MLIP [64], LAMMPS [65] and Materials Machine Learning (maml).

2.4. Analysis of the coupling of anion rotation and Li migration

To calculate the local difference frequency center (LDFC), the cluster rotational frequency ($f_{rotation} = \frac{1}{360} \times \frac{d(\theta_{s-o})}{dt}$) and the Li hopping frequency ($f_{hopping} = \frac{d_{max}}{d_{cut}t}$) were calculated during the MD simulation, the $\theta_{s\text{-}o}$ is the rotational angel for S-O bond compare to the initial position of S-O bond at time t, d_{cut} is determined by the first peak of RDF. And the Li atoms neighbor to the center atom (S) and edge atom (O) are considered for calculating the Li hopping frequency. Besides, the MD process is divided into many sections according to the time that the index of neighbored Li atoms changed. And the LDFC can be defined as the difference of averaged cluster rotational frequency and averaged Li hopping frequency.

3. Results and discussion

3.1. Structure and stability of the cluster-based anti-perovskites

In this work, we considered the APs structures by combining the Li, divalent A anions (including O^{2-}, S^{2-}, Se^{2-}, Te^{2-}, SO_4^{2-}, SeO_4^{2-}) and monovalent B anions (including F^-, Cl^-, Br^-, I^-, H^-, OH^-, CN^-, NO_2^-, NH_2^-, BH_4^-, BF_4^-, BCl_4^- and AlH_4^-) to form structures with the chemical formula of Li_3AB (Li_3BA). For the typical APs (Li_3AB, Fig. 1a), a anions form the corner-sharing Li_6A octahedra with the space between octahedra occupied by monovalent anions B. The corresponding predicted Goldschmidt tolerance factors (*t*) for these typical APs (Fig. S2) show that there are limited number of A-B pairs (17 pairs) with *t* in the optimal range of 0.8~1.1 for stable APs [26], in addition to 8 Li_3AB already studied before such as Li_3OCl and Li_3OBH_4, only 9 Li_3AB with the suitable *t*. On the contrary, the exchange of positions for anions A and B (forming modified-Li_3BA, namely m-Li_3BA, Fig. 1a) triggers more A-B pairs (28 pairs) to form the stable APs with *t* in the range of 0.8~1.1 (Fig. 1b), while few studies involve this m-Li_3BA. Thus, to explore this new fertile ground of site-exchanged antiperovskites for solid state electrolytes, we adopted global minimum search of free energy surfaces via DFT calculations (Experimental Section) to only predict the ground-state structures of cluster-based m-Li_3BA (also called PAPs) with *t* in the range of 0.8~1.1. The optimized ground-state structures are shown in Fig. S3 and the lattice constants are displayed in Table S1, whose structures have different degrees of distortion and exhibit the pseudo-cubic feature with high stability.

The calculated energy above hulls (E_{hull}) for m-Li_3BA listed in Table S2 further confirm that most single cluster-based APs are thermodynamically stable (E_{hull} =0, such as Li_3OHS, Li_3ClSeO_4, etc.), while there are relatively large E_{hull} values for double cluster-based APs. Considering the instabilities of anion polyhedron with possible rotations in the anti-perovskite framework, we focused on the PAPs with E_{hull} lower than 0.2 eV/atom to further explore the potential applications on the SSEs. Also, the E_{hull} is used as a criterion for the synthesizability as it determines the material's thermodynamic stability relative to other competing phases. We thus set a threshold of $E_{hull} < 0.2$ eV/atom to pick the potential APs based on the previous work, which suggests that the previously synthesized metastable materials have the changed Ehulls in the range of 0.05~0.2 eV/atom by an analysis in a curated set of ~30,000 inorganic materials obtained from the Materials Project database [27]. Therefore, the predicted thermodynamically stable structures with $E_{hull} = 0$, such as Li_3OHX (X = S, Se and Te) and Li_3YSeO_4 (Y = Cl, Br and I), are likely to be synthesizable (phase diagrams are also constructed, Fig. S4). Besides, the phonon dispersions (Figs. 1c and S5) indicate these metastable materials are dynamically stable and these materials may be thermodynamically stable by the entropic contributions at elevated temperatures. Therefore, the temperature-dependent formation free energies (section S1) were calculated to further confirm the confirm the synthesizability. As indicated in Fig. S6, these predicted structures, such as Li_3YSO_4 (Y = Cl, Br and I), are entropically stable at elevated temperatures and much likely to be experimentally synthesized. Notably, for the Li_3OHX (Figs. 1c and Fig. S5, X represents the element of S, Se, Te), the imaginary phonon modes at R points represent the rotations of Li_6O octahedron, which may have few influences on the stabilities of anion frameworks. Actually, these rotation modes may have potential contributions to the superionic conductivities, which have been discussed by recent studies conducted by Kageyam's group [28]. For the $Li_3NH_2SO_4$, the imaginary phonon modes represent the rotations of NH_2^- groups, which modes may facilitate the paddlewheel mechanism for the greater ionic conductivity.

The band structures for stable PAPs are calculated based on the HSE06 hybrid functional to predict the upper boundaries of electrochemical stabilities, as shown in Fig. S7. The calculated band gaps for PAPs are in the range of 3.93~8.14 eV (Fig. 1d), which are larger than most of sulfides and comparable with oxides as indicated in Fig. 1e,

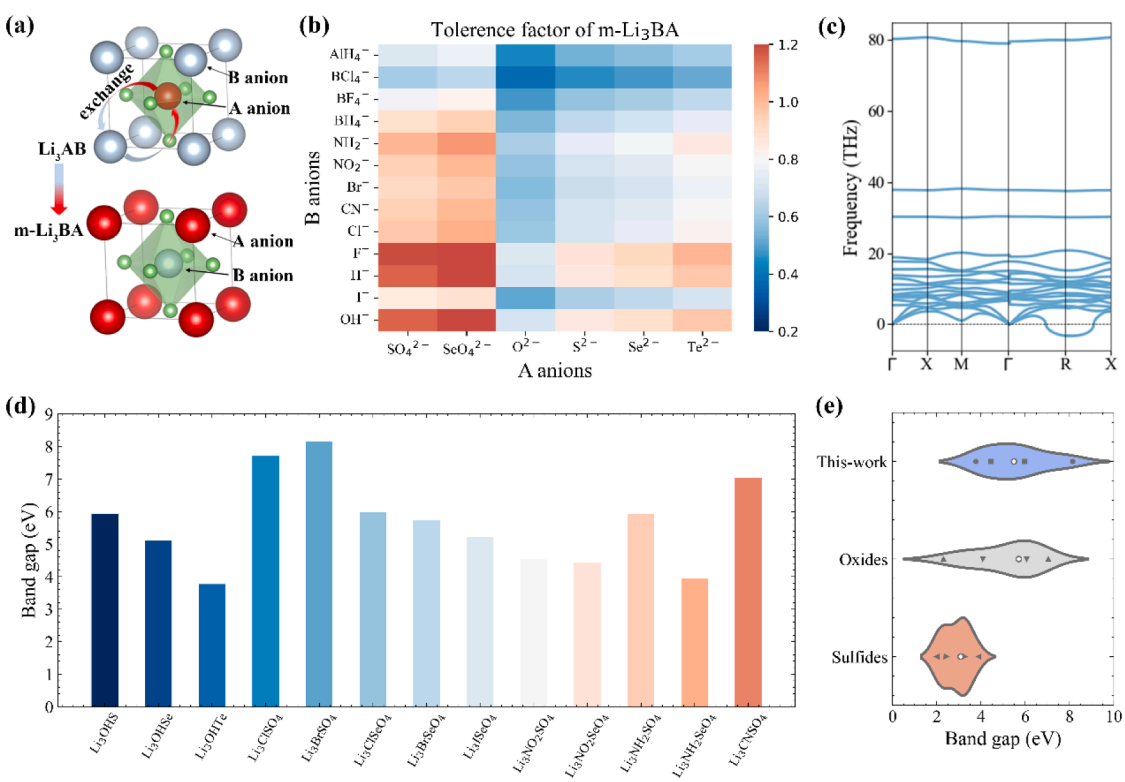

Fig. 1. (a) The schematic for exchanging positions of A and B anions to form the modified-Li_3BA (m-Li_3BA). (b) Heat maps of the predicted tolerance factors of m-Li_3BA, the horizontal axis represents the divalent anions A and vertical axis represents the monovalent anions B. (c) The phonon dispersion of the Li_3OHS. (d) The band gaps of the stable m-Li_3BA calculated by HSE06 hybrid functional. (f) The comparison of the band gaps of PAP, oxide and sulfide SSEs [30–43].

reducing the possibility of electron leakage during the operation of battery. The calculated band gap of Li_3OCl (6.25 eV) agrees well with the previous theoretical study (6.2 eV) [29].

3.2. Ionic conductivities of the cluster-based anti-perovskites

Based on AIMD simulations in the range of 600~1200 K, the Arrhenius relations, fitted activation energies (E_a) and extrapolated room-temperature conductivities (σ_{RT}) have been obtained, as displayed in Fig. 2a and Fig. S8a. All the designed structures with low activation energies (0.22~0.38 eV) and high ionic conductivities (0.04 ~ 10.91 mS/cm) show the superior ionic conductivities than typical APs, such as Li_3OCl (σ_{RT} = 0.021 mS/cm, details can be found in Fig. S9, and the result is consistent well with the earlier computational work [44]) or Li_3OBr (σ_{RT} = 0.00724 mS/cm) [44], implying the great potential as SSEs. Li_3BrSO_4, $Li_3NO_2SO_4$ and Li_3OHTe (σ_{RT} = 10.91 mS/cm, 5.26 mS/cm and 6.7 mS/cm, respectively) show the comparable room-temperature ionic conductivities with some sulfide SSEs, i.e, $Li_{3.45}Si_{0.45}P_{0.55}S_4$, σ_{RT} = 6.7 mS/cm [45]. The high ionic conductivities were also confirmed by the probability density distributions of Li ions based on the AIMD simulations. As displayed in Fig. S8b, the 3-dimensional (3D) Li diffusive channels are formed by the distinct Li crystallographic sites in the Li_6X octahedron, and the even density distribution suggests that there is relatively flat energy landscape for Li ion diffusion. The 3D Li ion diffusion in PAPs is also verified from the isotropic mean square displacements (MSD) of Li ions (Figs. 2b and S10) at 900 K. However, the existence of grain boundaries (GB) may result in the difference of ionic conductivity between single crystals and polycrystals. According to the previous reports [46], the influence of the GB on the total ion conductivity is strongly depending on the materials system, so it is difficult for us to determine a priori whether GBs will be detrimental or beneficial for the total ionic conductivities of our predicted materials. But it is not the highlight in the study, we will focus on this influence in our future study. In addition, to further verify the extrapolated RT ionic conductivity, the machine learning atomic potential based on the moment tensor potential (MTP) framework for Li_3BrSO_4 was trained in this work, detailed process and parameters are shown in Section S1. The mean absolute errors (MAEs) in energy and force are 2.25 meV/atom (Fig. 2c) and 0.09 eV/Å (Fig. S11), which are similar to or less than those of other MTPs fitted in the previous work [47], showing the high accuracy of reproducing DFT energies and forces. The ultralong-time MD simulation (1 μs) at room temperature (300 K) was conducted by this machine learning potential. The total MSD of Li ion diffusion in Li_3BrSO_4 is shown in Fig. 2d, the corresponding diffusion coefficient is 6.2×10^{-8} cm^2/s, much close to the DFT extrapolated RT diffusion coefficient (6.96×10^{-8} cm^2/s), confirming the accuracy of DFT predicted RT ionic conductivities. Also, the MSD for O ions (Fig. S11b) exhibits the low-temperature rotatability of SO_4^{2-} anions during a microsecond level.

By analyzing the dynamics of lithium ions during the AIMD simulations, PAPs with high ionic conductivities, such as Li_3BrSO_4 and Li_3OHTe, display the weak time correlations for Li ions hopping based on the van Hove correlation function (Fig. S12), indicating that the concerted migration has few contributions to the ionic conductivities of PAPs. Besides, radius distribution functions (RDFs) provide the valuable structural information to shed light into the diffusion bottleneck. For instance, the RDFs (Fig. S13) of Li_3BrSO_4 (σ_{RT} = 10.91 mS/cm) and Li_3BrSeO_4 (σ_{RT} = 0.15 mS/cm) indicate that the averaged bond lengths of Li-O and Li-S ionic pairs are same in the both structures (or Li-O, Li-N, Li-S and N-O pairs in $Li_3NO_2SO_4$ and $Li_3NO_2SeO_4$, σ_{RT} = 5.3 mS/cm and 0.8 mS/cm, respectively), and only little difference can be found between Li-S (3.15 Å) and Li-Se (3.31 Å) pairs caused by different elements, which are not enough to explain the large change of ionic conductivities. Thus, the Coulombic interactions are also not the dominant mechanism for fast cations diffusion in these PAPs.

To further probe the features for the high ionic conductivities of PAPs (taking Li_3BrSO_4 system as an example), the MSD curves for every element has been studied (see Fig. S14a). It is worth noting that there are certain displacements of edged ions of anion clusters (as the O ions in the SO_4^{2-} clusters in Fig. 2e, MSDs for other PAPs are shown in Fig. S15), while the MSDs for these edged ions become flatten gradually with time, which means these edged ions diffuse in a limited space. To visualize this interesting phenomenon, the ion migration trajectories of Li_3BrSO_4 from the 900 K AIMD simulations show that the oxygen atoms only move around the sulfur atoms without any obvious long-range migration,

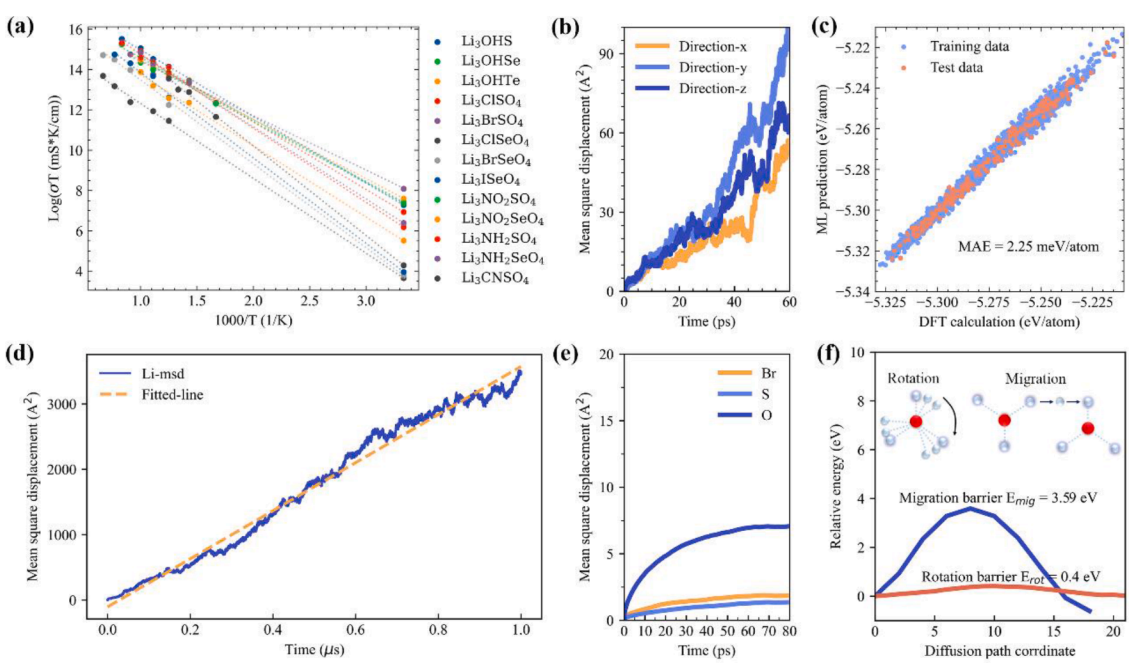

Fig. 2. (a) Calculated Arrhenius relations based on AIMD simulation for Li diffusion in studied PAPs. (b) The mean square displacement (MSD) for Li in Li_3BrSO_4 along x, y and z directions. (c) Comparisons of the energies obtained by MTP and DFT on the training and testing dataset for Li_3BrSO_4. (d) The MSD for Li in Li_3BrSO_4 based on the ultralong-time MLMD simulations (1 μS). (e) The MSD for Br (orange), S (light blue) and O (drak blue) in Li_3BrSO_4. (f) The calculated anion rotation and migration barriers, E_{rot} and E_{mig}, based on NEB calculation for Li_3BrSO_4. The inset plot shows the schematic of anion rotation and migration.

suggesting the rotational dynamics of anion clusters in PAPs (see Fig. S14b and c). The possibility of this anion rotation mode was assessed by the bond valence pathway analyzer (BVPA) [48], E_{rot} and E_{mig} represent the energy barrier of anion rotation in a cluster and anion migration between neighbor clusters respectively. For PAPs in this work, the E_{rot} is always smaller than E_{mig} (Fig. S16), indicating that the rotation mode occurs prior to migration mode. Also, we adopted the climbing image nudged elastic band (CI-NEB) method [49] to calculate the both energy barriers (E_{rot} and E_{mig}) of SO_4^{2-} in Li_3BrSO_4 (Fig. 2f) (the detailed information for this CI-NEB is provided in Section S2). NEB result indicates the low energy barrier for the rotation of SO_4^{2-} and the relatively large barrier for the migration mode, which agrees well with the BVPA calculation.

3.3. Dynamics properties

The observed anion rotations in PAPs may be responsible for the high ionic conductivities by providing extra power for Li migration. Therefore, to understand the dependence of the Li-ion conductivity on the rotation dynamics of anions or the potential correlations between Li diffusion and anion rotations, we first determined the non-trivial diffusion events by a protocol previously adopted to characterize Li dynamics in LLZO or in glassy Li_3PS_4 [50,51], which identifies the long-lived Li-ion displacements (events) during the AIMD simulations by analyzing the functional:

$$h_i(t;t_p,a,t_a) = \prod_{t'=(t_a-t_p)/2}^{t_a/2} \theta(|r_i(t+t') - r_i(t-t')| - a)$$

This functional is performed for each Li ion (i) in the snapshot structure at time t, and $h_i = 1$ suggests the ion i undergoes a long-lived displacement. $\theta(x)$ represents the Heaviside step function, which equals to 0 or 1 when the displacement ($|r_i(t+t') - r_i(t-t')|$) less or larger than a. Thus, only the migrations with displacements $\geq a$ that occur over a time $\leq$ ($t_w = t_a - t_p$) and stay at a distinct position for a time $\geq t_p$ are picked out, t_p is the residence time before and after the displacement event, t_w is the transition time and t_a is the time window including the residence and transition times. In the current work, 3 ps and 12 ps of t_w and t_a were adopted to explore the long-lived Li-ion large-displacement events. In addition, the values of a for different structures can be chosen according to the RDF of Li-Li pairs, which correspond to the minimal bond length of Li-Li pairs [52].

The identified long-lived Li diffusion events are characterized by plotting the h_i vs. time for every Li ion in the simulated supercell (23 Li ions). Fig. 3a displays the diffusion events for Li migration in the Li_3BrSO_4, among which 18 distinctive events with significant time

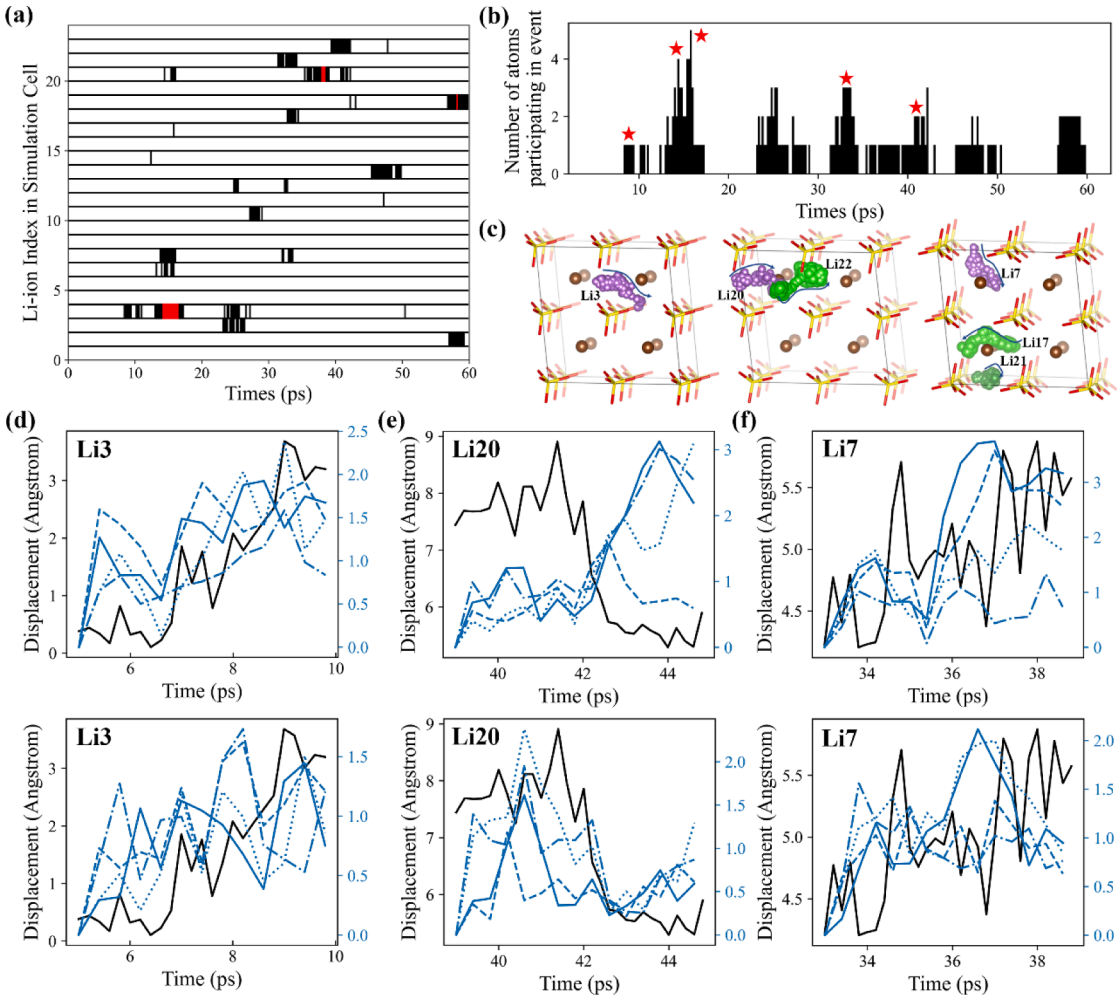

Fig. 3. Characterization of the long-lived Li-ion migration in Li_3BrSO_4. (a) The Li-ion migration events identified from the AIMD simulation during 60 ps, with 23 Li ions. For instance, for the 20th Li-ion (corresponding to the line at '20'), an event will be recorded which starts at about 15 ps, the red region represents the events with a larger threshold distance (a = 4 Å). (b) Number of Li ions participates in a diffusion event at the same time. (c) The trajectories of specific Li ions for events marked by red stars in (b), including one, two and three Li ions participate in a diffusion event. (d–f) The line displacements of the Li ion (black line) and the O ions (blue lines) in two neighboring SO_4^{2-} anion clusters for events shown in (c).

interval can be found, and there are more events with a smaller threshold distance a (shown in Fig. S17). Although there are in general subtle differences of threshold distance for different structures, the significantly more events (also, more events with larger threshold distance of $a = 4$ Å marked as red region in Fig. 3a indicate the longer migration pathway with low activation energy) were found in the high Li ion conducting Li_3BrSO_4 compared to other PAPs, such as Li_3ClSO_4, Li_3BrSeO_4, Li_3ISeO_4 and $Li_3NO_2SO_4$ (see Figs. S18 and S19).

Summing the h_i at each time effectively identifies the number of Li ions whose long-lived diffusion events occur near simultaneously. These events are displayed in Figs. 3b and S18–19, mainly involving the participation of one, two and three Li ions during the same time windows (also, four or five Li ions participation can be found in Li_3BrSO_4). Fig. S20 plots summed h_i versus varied parameters (residence time Δt and time window t_a), which shows that the time correlated migration events persist across the range of varied parameters and demonstrates that the qualatitive migration behaviors are not sensitive to the detailed sampling procedure. Although the events of Li-ion migrations are correlated in time based on the above analysis of h_i, whether these events are correlated in space is not clear. To address this question, we illustrated the real-space displacements of Li (Li-ions diffusion trajectories) in Li_3BrSO_4 for specific diffusion events marked by red stars in Fig. 3b as displayed in Fig. 3c. Noting that, only few Li diffusion events exhibit the correlation in space, such as Li20 and Li22 of Li_3BrSO_4 in Fig. 3c. The involved two adjacent Li ions undergo migrations that impinge upon the previous positions of the others, which is reminiscent of the ion migration in glass that always involves the cooperative migration correlated in space and time [53]. While there are more Li migration events in PAPs without the correlation in space (such as the events involved Li7, Li17 and Li21 of Li_3BrSO_4 in Fig. 3c), these Li ions are correlated in time. This is different from the diffusion behaviors in traditional anti-perovskite SSEs (Li_3OCl), as previous work reported by Zerina [54] that the correlated migration dominates the Li-ions diffusive behaviors.

Most importantly, the present work highlights that the reorientations of anion clusters will occur simultaneously with the Li diffusion events, are these reorientations contributing to the fast Li-ion migrations in PAPs? Fig. 3d-f illustrate the displacements of Li ions and neighboring anions rotations in Li_3BrSO_4 to answer this question, which are relative to the initial positions of ions in the range of chosen time windows for specific migration events marked by red stars in Fig. 3b. For the case of one, two and three-ions migration events in Li_3BrSO_4, the rotational displacements of SO_4^{2-} are significantly synchronized with the migration of lithium cation (Li3, Li20 and Li7) during the same time windows (Fig. 3d–f), the corresponding anion rotational displacements can reach 3.0 Å, showing large rotational angles. Also, the similar correlation between the displacements of cations and rotation of anion clusters are found in other PAPs (Fig. S18–19, S21). Fig. S22 provides a more detailed view of this coupling diffusion mechanism by highlighting how the anion clusters (nearest neighbors to migrating Li ion) rotate in a Li

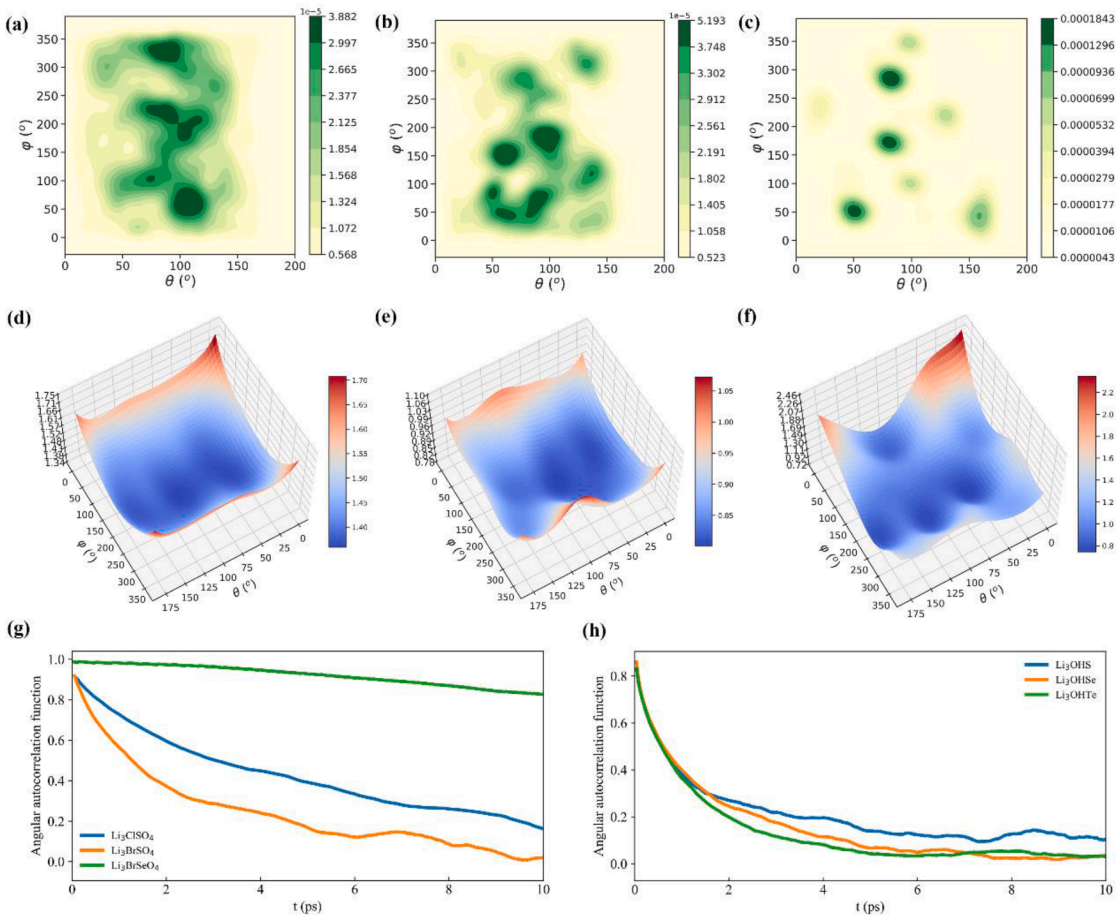

Fig. 4. The 2 dimensional probability density distributions (a-c) and the Helmholtz free energy surfaces (d–f) of the clusters in Li_3BrSO_4, Li_3ClSO_4 and Li_3BrSeO_4, respectively. The positions and heights of the local minima and the transition states in the Helmholtz free energy surfaces display the rotational pathways and barriers. The angles of θ and φ are defined in the reference framework of the lattice structures, the angles between S-O bond and the z axis or between the x axis and the projection of the S-O vector in the xy-plane are defined as the θ or φ. The schematic can be seen in the Fig. S23. (g) The angular autocorrelation functions for clusters (SO_4^{2-} and SeO_4^{2-}) in the Li_3BrSO_4, Li_3ClSO_4 and Li_3BrSeO_4 systems during the AIMD simulations. (h) The angular autocorrelation functions of OH^- in the Li_3OHS, Li_3OHSe and Li_3OHTe systems.

diffusion event. In all of the displayed migration events, the anion clusters exhibit the same displacement direction with the Li migrations, implying the faster Li migrations promoted by anion rotations. Therefore, based on the above analysis, it is reasonable to conclude that the anion cluster rotations are highly correlated with the Li migrations in space and in time in PAPs, which is consistent well with the paddlewheel-type mechanism.

For exploring how the anion cluster rotation dynamics affect the Li-ion migration, AIMD data were further extracted to calculate the 2-dimension probability density distributions and the Helmholtz free energy surfaces of the anion clusters. As illustrated in Fig. 4a–c, based on the spherical coordinates (for defining the angles θ and φ of anion clusters and evaluating the rotational angles during the simulation process, the schematic can be seen in Fig. S23), the 2D density distributions of S-O and Se-O bonds in Li_3BrSO_4, Li_3ClSO_4 and Li_3BrSeO_4 (the three similar structures with relatively large difference of ionic conductivities were selected as examples) reveal the dispersive and disordered rotation of anion clusters with varied angles θ and φ, exhibiting the anion reorientation dynamics. The distinct maxima of density distributions for four O atoms bonded to S exhibit the higher probability density distribution than that of SeO_4^{2-}, suggesting the significant and negligible reorientation dynamics of SO_4^{2-} and SeO_4^{2-}, respectively. This is consistent well with the displacements results (Fig. S18b), showing that O atoms in SeO_4^{2-} anions exhibit smaller displacements than that in SO_4^{2-} anions during the studied migration events. Fig. 4g demonstrates a quantitative measure of the rotation dynamics of anion clusters (angular autocorrelation function C(t), see Section S1 for details), the faster decay of the anion reorientation reveals the greater rotational freedom for SO_4^{2-} in Li_3BrSO_4 (the decay of anion reorientation follows the trend, SeO_4^{2-} (Li_3BrSeO_4) < SO_4^{2-} (Li_3ClSO_4) < SO_4^{2-} (Li_3BrSO_4)), attributing to the flatter rotational free energy landscapes for O ligands of the SO_4^{2-} anions with the low Helmholtz free energy barriers of 0.15–0.25 eV (Fig. 4d-e) than O ligands of the SeO_4^{2-} anions (higher Helmholtz free energy barriers of 0.5–0.6 eV, Fig. 4f). Noting that the C(t) for SeO_4^{2-} anions in Li_3BrSeO_4 is approximately near 0.8, signifying that the anion rotations are oscillatory around their initial positions. Similarly, the SeO_4^{2-} anions in Li_3ClSeO_4 and Li_3ISeO_4 also exhibit the low rotational dynamics, yet the other studied systems exhibit the relative high anion-rotation dynamics illustrated by the angular autocorrelation functions in Fig. S24. This limited rotational freedom of SeO_4^{2-} demonstrates the main reason for its low RT ionic conductivity (0.146 mS/cm of Li_3BrSeO_4, which is far less than 10.91 mS/cm of Li_3BrSO_4), namely the slow rotational dynamics weakening the paddlewheel effects and thus slowing the Li migration [55].

3.4. Dynamics coupling between anion cluster and cations

However, the rotational freedom alone not nessesarily guarantees the paddlewheel phenomenon for high ionic conductivities. As demonstrated in Fig. 4h, the faster decay of angular autocorrelation functions for OH anions in Li_3OHX (X represents the S, Se and Te) exhibit the faster rotational dynamics than SO_4^{2-} in Li_3BrSO_4, while the ionic conductivities of Li_3OHX are lower than that of Li_3BrSO_4. Thus, the possible effects from the dynamics coupling between anion cluster and cations was further discussed in the following.

According to the discussion of previous work [24], besides the rotational freedom, the occurred time scale of rotational modes causing the energy landscape fluctuation (frequency associated with the rotational dynamics) is also a crucial factor for accelerating the migration rate of cations based on the paddlewheel mechanism, and too fast or too slow fluctuation will weaken the paddlewheel effect. In this work, the power spectra (vibration density of states) for cations and anions were calculated from the velocity autocorrelation function to characterize the time scales or fluctuations. Several qualitative features are noteworthy according to the power spectra displayed in Fig. S25. Firstly, some PAPs with the greater ionic conductivity display lower-frequency peak. For example, the lithium vibrational spectrum of Li_3OHX shifts to lower frequency when X changes from S to Te with the increased ionic conductivities. This phenomenon is in agreement with the theory argued by Muy et al [56], which reported that the density of low-frequencies lithium modes is correlated with the probability for lithium migration. However, the lithium vibrational spectra of Li_3BrXO_4 and Li_3ClXO_4 (X is the S and Se) show the opposite feature (Fig. S25), i.e., the $Li_3Br(Cl)SO_4$ exhibits the greater ionic conductivity and the higher-frequency peak compared to that of Li_3XSeO_4 (X is the Cl, Br and I), the corresponding average vibrational frequencies are 289.89 (295.08) cm^{-1} for $Li_3Br(Cl)SO_4$ and 272.69∼284.02 cm^{-1} for Li_3XSeO_4. A similar phenomenon has been also reported in brominated Li_3OCl systems [57], suggesting that the paradigm of "lower lithium phonon band center is accompanied by the higher ionic conductivity" may not be straightforward as previously thought for PAPs.

In addition, as identified in Fig. S26, the overlap between Li and anions vibrational spectra suggest that the momentum transfer occurs between the dynamics of anion clusters and lithium, which provides the additional driving force for the migration of lithium. Thus, the PAPs exhibiting the significant paddle-wheel effects to assist the Li migration shall possess the strong vibrational coupling and the large anion reorientations. While for Li_3XSeO_4 systems, the low rotational freedoms of SeO_4^{-2} (Figs. 4g and S26) weaken the paddlewheel effect although the obvious vibrational coupling can be found between SeO_4^{-2} and Li. Finally, the local difference frequency center (LDFC, Computation Methods) is defined to evaluate the coupled degree of Li hopping and cluster rotation in a more quantatitive way, which can be calculated as the difference of the average anion cluster rotational frequency and the average Li hopping frequency, see details in Method. The corresponding kernel density distributions of $f_{rotation}$ and $f_{hopping}$ for Li_3BrSO_4 are shown in Fig. 5a. It shall be noted that only the Li atoms neighboring to the studied clusters are considered for the statics of $f_{hopping}$ and the smaller LDFC indicates the higher coupled degree of Li hopping and cluster rotation (see similar results for other PAPs in Fig. S27). It can be seen from Fig. 5b that the Li_3BrSO_4 with the minimum LDFC (1.64) shows the strongest coupling between Li and SO_4^{2-} dynamics, thus exhibiting the lowest activation energy. In summary, the increased LDFC suggests the reduced paddlewheel dynamics, which correspond to the lower ionic conductivity in some studied PAPs in this work. Therefore, our LDFC can be generally applied to provide a unified physical picture for the contributions of paddlewheel mechanism on the enhanced Li migration across many super-ionic conductors with anion rotation dynamics.

4. Conclusion

In this work, using a combination of particle swarm optimization algorithm and DFT simulations, we demonstrated the exchanging anion lattice sites in the anti-perovskite could promote the structure stabilities for incorporating anion clusters and ionic conductivities simultaneously. The structure stabilities were characterized by energy above hull and phonon spectrum (showing the thermodynamically and kinetically stability, respectively), and the calculated ionic conductivities of these PAPs are comparable with some sulfide SSEs, among which the promising Li_3BrSO_4 (σ_{RT} = 10.91 mS/cm) shows the highest ionic conductivity, which is hundreds of times higher than the ionic conductivity of typical Li_3OCl antiperovskite, 0.0248 mS/cm. Additionally, we detected that the obvious rotational dynamics of anion clusters for most PAPs, the further dynamics analysis indicate that anion cluster rotations of PAPs with high ionic conductivity are highly correlated with the Li migrations in space and in time, exhibiting the strong paddlewheel-type dynamics. Importantly, the local difference frequency center (LDFC) was proposed to quantitatively evaluate the strength of paddlewheel dynamics, and Li_3BrSO_4 with the minimum LDFC (1.64 THz) shows the lowest activation energy. Thus, we conclude that the cluster-based anti-perovskites with high ionic conductivity exhibit the several key features that enable

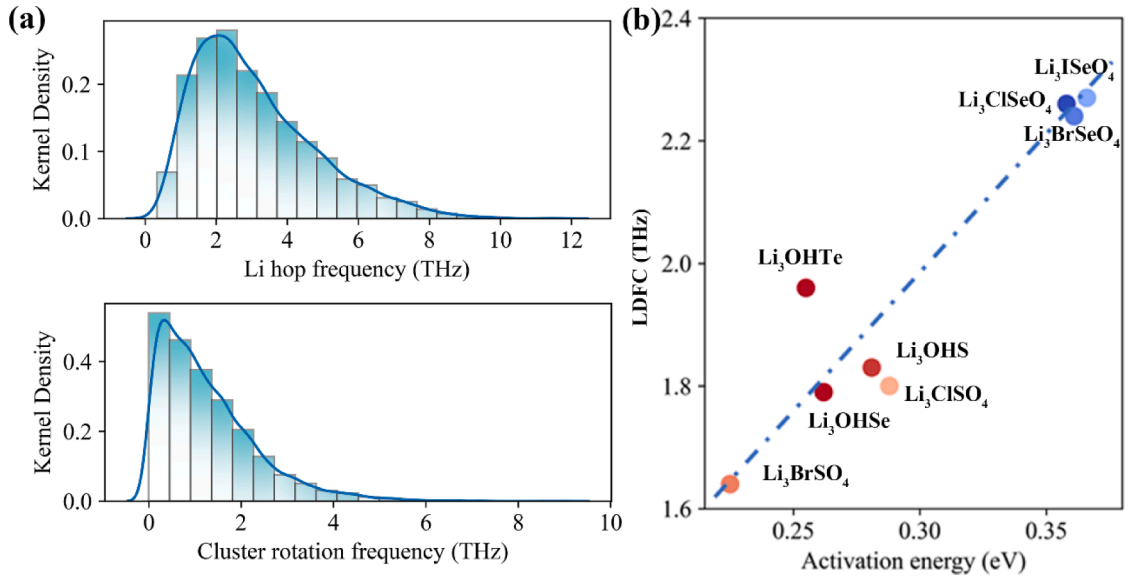

Fig. 5. (a) The kernel density distribution of Li hop frequency and cluster rotation frequency for Li_3BrSO_4 structure during MD simulation at 900 K. (b) The local difference frequency center (LDFC) versus activation energies for different structures. The red (blue) datapoint represents the PAPs with the faster (slower) decay rate of anion reorientation.

the paddlewheel dynamics. Firstly, these structures contain anion clusters with the high rotational freedom to potentially drive the Li migration. Then, these structures shall also display the small LDFC for strong coupling degree between Li migration and anion rotational modes. In general, these data demonstrate that the free-rotating anion clusters and the LDFC can be the structural and dynamics descriptors for screening or designing the novel fast ionic conductors with paddlewheel effects. We suggest more experiments and computations to study such Li-anion clusters rotational/vibrational coupling dynamics in the SSEs, which is the fertile ground in designing solid-state electrolytes.

Supporting Information (SI).

The method for calculating ionic conductivity, orientational correlation function and other supporting information.

CRediT authorship contribution statement

Chaohong Guan: Conceptualization, Investigation, Methodology, Data curation, Writing – original draft. **Yu Yang:** Methodology, Investigation. **Runxin Ouyang:** Methodology, Investigation. **Huirong Jing:** Methodology. **Jieqiong Yan:** Investigation. **Guoyao Li:** Investigation. **Huanan Duan:** Investigation. **Hong Zhu:** Resources, Supervision, Writing – review & editing.

Declaration of Competing Interest

The authors declare that they have no known competing financial interests or personal relationships that could have appeared to influence the work reported in this paper.

Data availability

Data will be made available on request.

Acknowledgments

This work was supported by National Natural Science Foundation of China (52072240), and the Materials Genome Initiative Center at Shanghai Jiao Tong University. All simulations were carried out with computational resources from Shanghai Jiao Tong University High Performance Computing Center.

Supplementary materials

Supplementary material associated with this article can be found, in the online version, at doi:10.1016/j.ensm.2023.102936.

References

[1] J.C. Bachman, S. Muy, A. Grimaud, H.H. Chang, N. Pour, S.F. Lux, O. Paschos, F. Maglia, S. Lupart, P. Lamp, L. Giordano, Y. Shao-Horn, Inorganic Solid-State Electrolytes for Lithium Batteries: Mechanisms and Properties Governing Ion Conduction, Chem. Rev. 116 (2016) 140.
[2] R. Chen, Q. Li, X. Yu, L. Chen, H. Li, Approaching Practically Accessible Solid-State Batteries: Stability Issues Related to Solid Electrolytes and Interfaces, Chem. Rev. 120 (2020) 6820.
[3] X. Li, J. Liang, X. Yang, K.R. Adair, C. Wang, F. Zhao, X. Sun, Progress and perspectives on halide lithium conductors for all-solid-state lithium batteries, Energy Environ. Sci. 13 (2020) 1429.
[4] N. Kamaya, K. Homma, Y. Yamakawa, M. Hirayama, R. Kanno, M. Yonemura, T. Kamiyama, Y. Kato, S. Hama, K. Kawamoto, A. Mitsui, A lithium superionic conductor, Nat. Mater. 10 (2011) 682.
[5] R. Murugan, V. Thangadurai, W. Weppner, Fast lithium ion conduction in garnet-type $Li_7La_3Zr_2O_{12}$, Angew. Chemie. Int. Ed. 46 (2007) 7778.
[6] M.A. Kraft, S.P. Culver, M. Calderon, F. Bocher, T. Krauskopf, A. Senyshyn, C. Dietrich, A. Zevalkink, J. Janek, W.G. Zeier, Influence of Lattice Polarizability on the Ionic Conductivity in the Lithium Superionic Argyrodites Li_6PS_5X (X = Cl, Br, I), J. Am. Chem. Soc. 139 (2017) 10909.
[7] H. Fang, P. Jena, Argyrodite-type advanced lithium conductors and transport mechanisms beyond peddle-wheel effect, Nat. Commun. 13 (2022) 2078.
[8] Y. Zhao, L.L. Daemen, Superionic conductivity in lithium-rich anti-perovskites, J. Am. Chem. Soc. 134 (2012) 15042.
[9] W.D. Richards, Y. Wang, L.J. Miara, J.C. Kim, G. Ceder, Design of $Li_{1+2x}Zn_{1-x}PS_4$, a new lithium ion conductor, Energy Environ. Sci. 9 (2016) 3272.
[10] A. Despotuli, Rambaby Nanoionics of advanced superionic conductors, Ionics 11 (2006) 306.
[11] S. Geller, J.R. Akridge, S.A. Wilber, Crystal structure and conductivity of the solid electrolyte α-$RbCu_4Cl_3I_2$, Phys. Rev. B 19 (1979) 5396.
[12] Y.J. Nam, D.Y. Oh, S.H. Jung, Y.S. Jung, Toward practical all-solid-state lithium-ion batteries with high energy density and safety: Comparative study for electrodes fabricated by dry- and slurry-mixing processes, J. Power Sources 375 (2018) 93.
[13] L. Barroso-Luque, Q. Tu, G. Ceder, An Analysis of Solid-State Electrodeposition-Induced Metal Plastic Flow and Predictions of Stress States in Solid Ionic Conductor Defects, J. Eletrochem Soc. (2020) 167.
[14] Y. Wang, W.D. Richards, S.P. Ong, L.J. Miara, J.C. Kim, Y. Mo, G. Ceder, Design principles for solid-state lithium superionic conductors, Nat. Mater. 14 (2015) 1026.
[15] Y. Yang, H. Zhu, Effects of F and Cl Doping in Cubic $Li_7La_3Zr_2O_{12}$ Solid Electrolyte: A First-Principles Investigation, ACS Appl. Energy Mater. 5 (2022) 15086.

[16] R. Jalem, Y. Yamamoto, H. Shiiba, M. Nakayama, H. Munakata, T. Kasuga, K. Kanamura, Concerted Migration Mechanism in the Li Ion Dynamics of Garnet-Type $Li_7La_3Zr_2O_{12}$, Chem. Mater. 25 (2013) 425.
[17] T. Yajima, Y. Hinuma, S. Hori, R. Iwasaki, R. Kanno, T. Ohhara, A. Nakao, K. Munakata, Z. Hiroi, Correlated Li-ion migration in the superionic conductor $Li_{10}GeP_2S_{12}$, J. Mater. Chem. A 9 (2021) 11278.
[18] X. He, Y. Zhu, Y. Mo, Origin of fast ion diffusion in super-ionic conductors, Nat. Commun. 8 (2017) 15893.
[19] K. Jun, Y. Sun, Y. Xiao, Y. Zeng, R. Kim, H. Kim, L.J. Miara, D. Im, Y. Wang, G. Ceder, Lithium superionic conductors with corner-sharing frameworks, Nat. Mater. 21 (2022) 924.
[20] P.J. Hong Fang, Li-rich antiperovskite superionic conductors based on cluster ions, PANS 114 (2017) 11046.
[21] H. Fang, S. Wang, J. Liu, Q. Sun, P. Jena, Superhalogen-based lithium superionic conductors, J. Mater. Chem. A (2017) 13373.
[22] J.A. Dawson, T.S. Attari, H. Chen, S.P. Emge, K.E. Johnston, M.S. Islam, Elucidating lithium-ion and proton dynamics in anti-perovskite solid electrolytes, Energy Environ. Sci. 11 (2018) 2993.
[23] Z. Zhang, H. Li, K. Kaup, L. Zhou, P.N. Roy, L.F. Nazar, Targeting Superionic Conductivity by Turning on Anion Rotation at Room Temperature in Fast Ion Conductors, Matter 2 (2020) 1667.
[24] E. Ahiavi, J.A. Dawson, U. Kudu, M. Courty, M.S. Islam, O. Clemens, C. Masquelier, T. Famprikis, Mechanochemical synthesis and ion transport properties of Na_3OX (X = Cl, Br, I and BH_4) antiperovskite solid electrolytes, J. Power Sources 471 (2020) 228489.
[25] J.A. Dawson, T. Famprikis, K.E. Johnston, Anti-perovskites for solid-state batteries: recent developments, current challenges and future prospects, J. Mater. Chem. A 9 (2021) 18746.
[26] W. Xia, Y. Zhao, F. Zhao, K. Adair, R. Zhao, S. Li, R. Zou, Y. Zhao, X. Sun, Antiperovskite Electrolytes for Solid-State Batteries, Chem. Rev. 122 (2022) 3763.
[27] W. Sun, S.T. Dacek, S.P. Ong, G. Hautier, A. Jain, W.D. Richards, A.C. Gamst, K. A. Persson, G. Ceder, The thermodynamic scale of inorganic crystalline metastability, Sci. Adv. 2 (2016), e1600225.
[28] S. Gao, T. Broux, S. Fujii, C. Tassel, K. Yamamoto, Y. Xiao, I. Oikawa, H. Takamura, H. Ubukata, Y. Watanabe, K. Fujii, M. Yashima, A. Kuwabara, Y. Uchimoto, H. Kageyama, Hydride-based antiperovskites with soft anionic sublattices as fast alkali ionic conductors, Nat. Commun. 12 (2021) 201.
[29] Z. Wang, H. Xu, M. Xuan, G. Shao, From anti-perovskite to double anti-perovskite: tuning lattice chemistry to achieve super-fast Li+ transport in cubic solid lithium halogen–chalcogenides, J. Mater. Chem. A 6 (2018) 73.
[30] I.H. Chu, H. Nguyen, S. Hy, Y.C. Lin, Z. Wang, Z. Xu, Z. Deng, Y.S. Meng, S.P. Ong, Insights into the Performance Limits of the $Li_7P_3S_{11}$ Superionic Conductor: A Combined First-Principles and Experimental Study, ACS Appl. Mater. Interfaces 8 (2016) 7843.
[31] T. Thompson, S. Yu, L. Williams, R.D. Schmidt, R. Garcia-Mendez, J. Wolfenstine, J.L. Allen, E. Kioupakis, D.J. Siegel, J. Sakamoto, Electrochemical Window of the Li-Ion Solid Electrolyte $Li_7La_3Zr_2O_{12}$, ACS Energy Lett. 2 (2017) 462.
[32] K. Nam, H. Chun, J. Hwang, B. Han, First-Principles Design of Highly Functional Sulfide Electrolyte of $Li_{10-x}SnP_2S_{12-x}Cl_x$ for All Solid-State Li-Ion Battery Applications, ACS Sustain. Chem. Eng. 8 (2020) 3321.
[33] Z. Xu, H. Zhang, T. Yang, X. Chu, Y. Xie, Q. Wang, Y. Xia, W. Yang, Physicochemically dendrite-suppressed three-dimensional fluoridation solid-state electrolyte for high-rate lithium metal battery, Cell Rep. Phys. Sci. 2 (2021) 100644.
[34] Z. Zhu, I.H. Chu, S.P. Ong, Li3Y(PS4)2 and Li5PS4Cl2: New Lithium Superionic Conductors Predicted from Silver Thiophosphates using Efficiently Tiered Ab Initio Molecular Dynamics Simulations, Chem. Mater. 29 (2017) 2474.
[35] Z. Wang, G. Shao, Theoretical design of solid electrolytes with superb ionic conductivity: alloying effect on Li+ transportation in cubic Li_6PA_5X chalcogenides, J. Mater. Chem. A 5 (2017) 21846.
[36] T. Binninger, A. Marcolongo, M. Mottet, V. Weber, T. Laino, Comparison of computational methods for the electrochemical stability window of solid-state electrolyte materials, J. Mater. Chem. A 8 (2020) 1347.
[37] E. Kazyak, K.H. Chen, A.L. Davis, S. Yu, A.J. Sanchez, J. Lasso, A.R. Bielinski, T. Thompson, J. Sakamoto, D.J. Siegel, N.P. Dasgupta, Atomic layer deposition and first principles modeling of glassy Li_3BO_3–Li_2CO_3 electrolytes for solid-state Li metal batteries, J. Mater. Chem. A 6 (2018) 19425.
[38] Z. Xu, R. Chen, H. Zhu, A Li2CuPS4 superionic conductor: a new sulfide-based solid-state electrolyte, J. Mater. Chem. A 7 (2019) 12645.
[39] S. Nachimuthu, H.J. Cheng, H.J. Lai, Y.H. Cheng, R.T. Kuo, W.G. Zeier, B.J. Hwang, J.C. Jiang, First-principles study on selenium-doped $Li_{10}GeP_2S_{12}$ solid electrolyte: Effects of doping on moisture stability and Li-ion transport properties, Mater. Today Chem. 26 (2022) 101223.
[40] M. Amores, H. El-Shinawi, I. McClelland, S.R. Yeandel, P.J. Baker, R.I. Smith, H. Y. Playford, P. Goddard, S.A. Corr, E.J. Cussen, Li(1.5)La(1.5)MO(6) (M = W(6+), Te(6+)) as a new series of lithium-rich double perovskites for all-solid-state lithium-ion batteries, Nat. Commun. 11 (2020) 6392.
[41] H.M. Chen, C. Maohua, S. Adams, Stability and ionic mobility in argyrodite-related lithium-ion solid electrolytes, Phys. Chem. Chem. Phys. 17 (2015) 16494.
[42] M. Aykol, S. Kim, V.I. Hegde, S. Kirklin, C. Wolverton, Computational evaluation of new lithium-3 garnets for lithium-ion battery applications as anodes, cathodes, and solid-state electrolytes, Phys. Rev. Mater. 3 (2019) 025402.
[43] A. Moradabadi, P. Kaghazchi, Defect chemistry in cubic $Li_{6.25}Al_{0.25}La_3Zr_2O_{12}$ solid electrolyte: A density functional theory study, Solid State Ion. 338 (2019) 74.
[44] Z. Deng, B. Radhakrishnan, S.P. Ong, Rational Composition Optimization of the Lithium-Rich $Li_3OCl_{1-x}Br_x$ Anti-Perovskite Superionic Conductors, Chem. Mater. 27 (2015) 3749.
[45] L. Zhou, A. Assoud, A. Shyamsunder, A. Huq, Q. Zhang, P. Hartmann, J. Kulisch, L. F. Nazar, An Entropically Stabilized Fast-Ion Conductor$Li_{3.25}[Si_{0.25}P_{0.75}]S_4$, Chem. Mater. 31 (2019) 7801.
[46] K. Kawahara, R. Ishikawa, K. Nakayama, T. Higashi, T. Kimura, Y.H. Ikuhara, N. Y. Shibata, Y. Ikuhara, Fast Li-ion conduction at grain boundaries in $(La,Li)NbO_3$ polycrystals, J Power. Sources 441 (2019) 227187.
[47] Y. Zuo, C. Chen, X. Li, Z. Deng, Y. Chen, J. Behler, G. Csanyi, A.V. Shapeev, A. P. Thompson, M.A. Wood, S.P. Ong, Performance and Cost Assessment of Machine Learning Interatomic Potentials, J. Phys. Chem. A 124 (2020) 731.
[48] L.L. Wong, K.C. Phuah, R. Dai, H. Chen, W.S. Chew, S. Adams, Bond Valence Pathway Analyzer—An Automatic Rapid Screening Tool for Fast Ion Conductors within softBV, Chem. Mater. 33 (2021) 625.
[49] N.A. Zarkevich, D.D. Johnson, Nudged-elastic band method with two climbing images: finding transition states in complex energy landscapes, J. Chem. Phys. 142 (2015), 024106.
[50] J.G. Smith, D.J. Siegel, Low-temperature paddlewheel effect in glassy solid electrolytes, Nat. Commun. 11 (2020) 1483.
[51] M. Burbano, D. Carlier, F. Boucher, B.J. Morgan, M. Salanne, Sparse Cyclic Excitations Explain the Low Ionic Conductivity of Stoichiometric $Li_7La_3Zr_2O_{12}$, Phys. Rev. Lett. 116 (2016) 135901.
[52] Y. Yang, Z. Xu, C. Guan, R. Ouyang, H. Jing, H. Zhu, Activating paddle-wheel effect towards lower temperature in a new sodium-ion solid electrolyte $Na_{3.5}Si_{0.5}P_{0.5}Se_4$, J. Mater. Chem. A 11 (2023) 9555.
[53] C.D.J.F.D.W.K.S.J.P.P.H.P.S.C. Glotzer, Stringlike Cooperative Motion in a Supercooled Liquid, Phys. Rev. Lett. 80 (1998) 2338.
[54] Z. Mehmedovic, V. Wei, A. Grieder, P. Shea, B.C. Wood, N. Adelstein, Impacts of vacancy-induced polarization and distortion on diffusion in solid electrolyte Li_3OCl, Philos. Trans. A Math. Phys. Eng. Sci. 379 (2021) 20190459.
[55] C. Guan, Y. Yang, R. Ouyang, H. Jing, J. Yan, H. Zhu, Enhanced ionic conductivity of protonated antiperovskites via tuning lattice and rotational dynamics, J. Mater. Chem. A 11 (2023) 6157.
[56] S. Muy, J.C. Bachman, L. Giordano, H.H. Chang, D.L. Abernathy, D. Bansal, O. Delaire, S. Hori, R. Kanno, F. Maglia, S. Lupart, P. Lamp, Y. Shao-Horn, Tuning mobility and stability of lithium ion conductors based on lattice dynamics, Energy Environ. Sci. 11 (2018) 850.
[57] R. Chen, Z. Xu, Y. Lin, B. Lv, S.H. Bo, H. Zhu, Influence of Structural Distortion and Lattice Dynamics on Li-Ion Diffusion in $Li_3OCl_{1-x}Br_x$ Superionic Conductors, ACS Appl. Energy Mater. 4 (2021) 2107.
[58] Y. Wang, J. Lv, L. Zhu, Y. Ma, Crystal structure prediction via particle-swarm optimization,, Phys. Rev. B 82 (2010).
[59] G. Kresse, J. Furthmüller, Efficient iterative schemes for ab initio total-energy calculations using a plane-wave basis set, Phys. Rev. B 54 (1996) 11169.
[60] A. Togo, I. Tanaka, First principles phonon calculations in materials science, Scripta. Mater. 108 (2015) 1.
[61] P. Giannozzi, S. de Gironcoli, P. Pavone, S. Baroni, Ab initio calculation of phonon dispersions in semiconductors, Phys. Rev. B 43 (1991) 7231.
[62] P. Deák, B. Aradi, T. Frauenheim, Polaronic effects in TiO_2 calculated by the HSE06 hybrid functional: Dopant passivation by carrier self-trapping, Phys. Rev. B 83 (2011) 155207.
[63] J. Qi, S. Banerjee, Y. Zuo, C. Chen, Z. Zhu, M.L. Holekevi Chandrappa, X. Li, S. P. Ong, Bridging the gap between simulated and experimental ionic conductivities in lithium superionic conductors, Mater. Today Phys. 21 (2021) 100463.
[64] I.S. Novikov, K. Gubaev, E.V. Podryabinkin, A.V. Shapeev, The MLIP package: moment tensor potentials with MPI and active learning, Mach. Learn. 2 (2021), 025002.
[65] S. Plimpton, Fast Parallel Algorithms for Short-Range Molecular Dynamics, J. Comput. Phys. 12 (1995) 1.